

Measurement of the inner structure of turbidity currents by ultrasound velocity profiling

Jumpei Hitomi¹, Shun Nomura^{2,*}, Yuichi Murai¹, Giovanni De Cesare³, Yuji Tasaka¹, Yasushi Takeda⁴, Hyun Jin Park¹, Hide Sakaguchi²

¹Laboratory for Flow Control, Hokkaido University, Kita 13 Nishi 8, Kita-ku Sapporo 060-0808, Japan

²Japan Agency for Marine-Earth Science and Technology (JAMSTEC), 3173-25 Showa-machi, Yokohama 2360001, Japan

³Plateforme de Constructions Hydrauliques, EPFL, Station 18, CH-1015, Lausanne, Switzerland

⁴Laboratory for Food Research Engineering, ETH Zurich, Rämistrasse 101, Zurich CH-8092, Switzerland

ARTICLE INFO

Article history:

Received 3 March 2020

Revised 11 November 2020

Accepted 7 December 2020

Available online 13 December 2020

Keywords:

Turbidity current

Velocity field

Two-fluid model

Ultrasound Doppler velocity profiling,

Flume experiment

ABSTRACT

The inner velocity structure and particle concentration profile of opaque turbidity currents were measured simultaneously by ultrasound velocity profilers. Currents consisting of a quartz particle suspension were generated by using the lock-exchange method in a flume to experimentally reproduce the quasi-steady state of a turbidity current. A pair of ultrasound transducers captured the horizontal and vertical velocities from Doppler frequencies, and the particle concentration profile was extracted from the echo amplitude. The data obtained were analyzed in terms of momentum conservation according to the two-fluid model. We found that: i) the viscous and Reynolds shear stresses balance in the top half of the current; and ii) the lower border of the stress balancing appears around the depth of the maximum vertical density gradient. These findings indicate that the reduction of flow resistance inside the body region of the turbidity current is maintained downstream, which enables the current to transport particles over a long distance.

© 2021 The Authors. Published by Elsevier Ltd.

This is an open access article under the CC BY-NC-ND license (<http://creativecommons.org/licenses/by-nc-nd/4.0/>)

1. Introduction

Turbidity currents, driven by the density difference between a heavy particle-laden fluid and an ambient fluid, have been a great research subject for a long time, because these currents convey large amounts of sediment to downstream areas and form large-scale submarine structures as a result of sediment accumulation (Simpson, 1997; Mulder and Alexander, 2001). Studies of these currents are also critical to civil and marine engineering for the estimation of potential risks and management of environmental hazards (e.g. Piper et al., 1999, Peakall et al., 2000; De Cesare et al., 2001; McCaffrey et al., 2003; Talling et al., 2007, 2012; Dorrell et al., 2014; Kneller et al., 2016; and references therein). Chamoun et al. (2016) and Schleiss et al. (2016) pointed out the potential reservoir sedimentation problems and Oehy and

Schleiss (2007) and Oehy et al. (2010) evaluated the positive effects of artificial solid obstacles and inclined jet screens on unavoidable reservoir sedimentation. In nature, turbidity currents propagate several hundred or thousand kilometers along the sea floor, as has been known from marine geological studies since the 1960s (Kneller and Buckee, 2000, Meiburg and Kneller, 2010). Previous reports have investigated long-range sediment transport (e.g. Dorrell et al., 2014; Kneller et al., 2016; Luchi et al., 2018; Dorrell et al., 2019 and references therein). Recently, Azpiroz-Zabala et al. (2017) reported field measurements obtained by an acoustic Doppler current profiler in the Congo Canyon; currents with a maximum height of 45–80 m were generated six times in seven months and continued for 5 to 10 days. Simmons et al. (2020) noted that the retarding friction force of the flow was surprisingly low, meaning that previous models were likely to have underestimated the flow velocity and traveling distance. Xu et al. (2010, 2014), Xu (2010), and Symons et al. (2017) reported seasonally repeated events in Monterey Bay (California) and discussed their effects on the underwater terrain. To represent the flow systems observed in the field, Parker et al. (1986) theoretically explained the physical description

* Corresponding author: Shun Nomura, Dr. Eng. Research Institute for Value-Added-Information Generation, Japan Agency for Marine-Earth Science and Technology (JAMSTEC), 3173-25 Showa-machi, Yokohama, 236-0001, Japan. Phone: +81-45-778-5784

E-mail address: nomura.shun@jamstec.go.jp (S. Nomura).

of turbidity currents: sediments entrained from the seabed continuously supply potential energy to the current, enabling the current to persist over a long distance. Many other numerical studies have assessed the long-range sediment transport system of turbidity currents (Meiburg and Kneller, 2010 and references therein).

In parallel with field observations and numerical simulations, a number of laboratory studies have examined the inner structures of turbidity currents to understand long-range sediment transport systems (e.g. Sequeiros et al., 2010, 2018; de Leeuw et al., 2018; Eggenhuisen et al., 2019 and references therein). In the early stage, many lock-gate type experiments were conducted because of the ease of the experimental setup and the high consistency with numerical analysis (e.g. Kneller et al., 1999; Samothrakis and Cotel, 2006; Cenedese and Adduce, 2008). Several studies using lock-gate flumes have confirmed the crucial role of the initial and boundary conditions in generating effective buoyancy of an initially organized multi-layer density stratification (Gladstone et al., 2004; Amy et al., 2005). The aim of the majority of these laboratory experiments was to visualize the outline of the current; i.e. the border between the sediment-laden layer and the ambient fluid as a function of time and space. Several trials have been conducted to observe the inner flow structure of a density or particle-laden flow by laser Doppler velocimetry (Kneller et al., 1999) or by particle tracking velocimetry (Thomas et al., 2003). However, it is difficult to observe the inner parts of a particle-laden turbidity current because of its opacity; thus, insights into the inner flow dynamics are limited.

In contrast, acoustic measurement methods are applicable to opaque fluids, non-invasive, and measure a wide range of velocities. Thus, an ultrasound velocity profiler (UVP; e.g., Takeda, 1995) is an effective tool for turbidity currents, because it can measure the spatio-temporal velocity distribution along the ultrasonic beam. Several previous studies described the use of UVP for measuring the velocity profiles of turbidity currents in laboratory flumes (Baas et al., 2005; McCaffrey et al., 2003; Choux et al., 2005; Gray et al., 2006). Those studies arranged and traversed ultrasound transducers to detect the inflection points of the local velocity profile as well as the turbulence intensity. For example, to measure profiles along ultrasonic beams with high resolution, Oehy and Schleiss (2007), Oehy et al. (2010), Sequeiros et al. (2018), and Nomura et al. (2020) installed UVP transducers at specific angles to the flume bottom. Particle concentrations in those experiments were measured by local sampling of sediment fluids. Felix et al. (2005) carried out combined measurements of the velocity and concentration of turbidity currents by applying UVP and an ultrasonic high concentration meter to measure the velocity and concentration profile simultaneously.

Since 2005, the capability of UVP has been extended to enable measurement of dispersions and interfaces involved in multiphase flows (Murakawa et al., 2008; Murai et al., 2010; Hitomi et al., 2017; Park et al., 2019). For a flow with a high sediment concentration, the degree of attenuation of the ultrasound beam can be used to estimate the spatial distribution of the flow. For bubbles and oil droplets in water, reflection and attenuation theory can be used in combination to reconstruct the dispersion distribution, as examined by Murai et al. (2009), Dong et al. (2015), Su et al. (2017), and Shi et al. (2019). For solid particles much smaller than the ultrasound wavelength in water, the echo intensity and its attenuation has been recently discussed while also considering the acoustic impedance of the particles (Rice et al., 2014, 2015; Bux et al., 2017), thereby highlighting the potential for further innovative investigations using UVP.

In this study, we present an interpretation of the flow mechanism by making use of the precise measurements facilitated by the extended utility of the UVP and the framework of momentum conservation in multiphase flow. In the first half of this paper, we

explain the experimental facility used to produce the turbidity currents, the particle properties, and the details of the measurement method utilizing UVP. In the second half, we report the visualized flow characteristics and quantify the flow structure inside the main body of a turbidity current. Data analysis, coupled with basic equations of turbulent dispersed two-phase flow, provides the turbulent shear stress profile in the main body of the current, which is a key factor for understanding long-range current migration in natural systems.

2. Experimental Method

2.1. Experimental Facility and Conditions

A schematic diagram of the experimental facility is shown in Fig. 1. The test section is an inclined (1.38°) rectangle flume 4548 mm long, 210 mm high, and 143 mm wide. The side and bottom walls are made of smooth acrylic material, and the top boundary is a free surface. The front wall is transparent, whereas the back wall is coated with a non-reflective black film to produce a dark uniform background for the visual assessments. The region enclosed by a dotted line in Fig. 1 indicates the visualization area for capturing the interface between the turbidity current and ambient water. A lock gate made of a plastic plate is placed approximately halfway along the flume. As an initial condition, the left (higher) side of the flume is occupied by a particle-laden heavier fluid with bulk density ρ_H , while the right (lower) side is filled with tap water with density ρ_W as an ambient fluid. The temperature and density of tap water are almost constant, 8.0°C and 999.9 kg/m³, respectively; thus, the viscosity of water μ_W is 1.385 mPa·s. After gate opening, the heavier fluid intrudes under the ambient fluid with front velocity U_f because of the density difference between the two fluids. The horizontal rightward displacement of the current is defined as the x axis and the height from the bed is the y axis.

Quartz particles mainly composed of SiO₂ (Carlo Bernasconi S.A., Switzerland) were used as suspended particles in the left side of the flume. The particle-size distribution measured with a Mastersizer 3.0 (Malvern S.A., United Kingdom.) is shown in Fig. 2. The mean diameter of the particles is $d_{50} = 12.2 \mu\text{m}$. The specific gravity of the particles is 2.65, and the weighted settling velocity v_s in water can be estimated by Stokes' law as follows (Altinakar et al., 1996):

$$v_s = \sum_i \frac{d_{pi}^2 (\rho_p - \rho_w) g}{18 \mu_w} p_i \quad (1)$$

where d_{pi} , ρ_p , and g ($= 9.8 \text{ m/s}^2$) are the particle size, particle density, and gravitational acceleration, respectively. The value of v_s from Eq. (1) is 0.38 mm/s, which is too small for significant deposition to occur during the experiment; thus, sedimentation effects are negligible in this research. The volume fraction of quartz particles f_s in heavier fluid is 0.5%, resulting in the mixture density ρ_H being 1008 kg/m³.

Although we conducted a series of flume experiments with different types of particles, particle size distributions, and concentrations (i.e. 0.25%–2.00%), here we focus on quartz particles for the above-mentioned conditions because this setup well represents the quasi-steady structure inside the turbidity current within the limited downstream length of the flume.

2.2. Velocity Profile Measurement

As shown in Fig. 3, a single turbidity current can be roughly classified into two parts: the head region, which is in an unsteady state and generates particle uplift, and the body region, which exhibits quasi-stationary stratified layers following the head region. To measure the velocities in both regions, a pair of 4-MHz

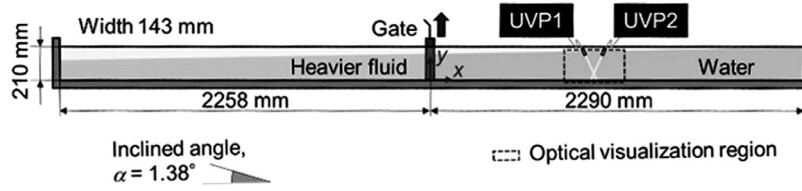


Fig. 1. Experimental apparatus used to generate and observe a turbidity current by the lock-exchange technique.

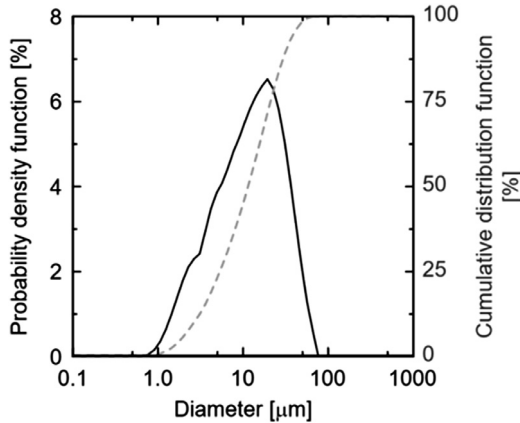


Fig. 2. Particle-size distribution of the quartz particles used in the flume experiments.

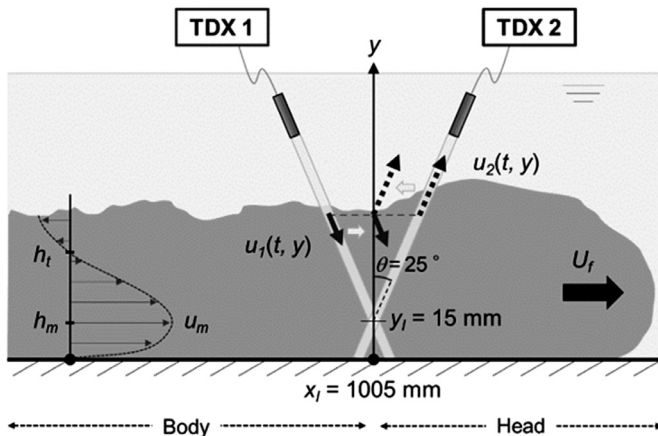


Fig. 3. Schematic diagram of the arrangement of ultrasound transducers, where u_m denotes the maximum streamwise velocity, $y = h_m$ is the corresponding height, and $y = h_t$ is the zero-crossing point.

UVP transducers is used, which has the advantage of measuring velocity profiles without mechanically traversing the transducers (Finelli et al., 1999; Dombroski and Crimaldi, 2007). The selection of instruments depends on the data to be extracted. In our approach, we employ UVP to resolve the vertical distributions of flow velocity and particle concentration, which is difficult to achieve using ADV (Acoustic Doppler velocimetry) (Cossu and Wells, 2012).

The transducers are installed at inclinations of $\theta = 25^\circ$ to the y axis and individually connected to two UVP Duo devices (Met-Flow S.A., Switzerland). In contrast to a multiplex system, this setup enables us to obtain two measurements simultaneously with no switching time. Two measurement lines along the transducers cross at $(x_1, y_1) = (1005 \text{ mm}, 15 \text{ mm})$. Here the intersectional height y_1 is selected to be almost the height of the maximum observed velocity obtained from preliminary tests. The starting time of the two-UVP measurement is synchronized with the gate opening.

Table 1

Parameters applied in the UVP measurement.

Basic frequency	4 MHz
Speed of sound in water	1480 m/s
Maximum velocity range	179.1 mm/s
Velocity resolution along the beam	1.399 mm/s
Maximum measurement length	358.2 mm
Number of channels	285
Number of profiles	4096
Sampling period for each profile	50 ms (20 Hz)
Window start	8.88 mm
Window end	219.04 mm
Wavelength (i.e. Channel distance)	0.74 mm
Special resolution	0.74 mm
Number of cycles	4
Repetition	32

The horizontal and vertical velocity components (u_1 and v_1) at the intersection are derived from the velocities along two measurement lines u_1 and u_2 as follows (Lhermitte and Lemmin, 1994):

$$u_1(y_1, t) = \frac{u_1(y_1, t) - u_2(y_1, t)}{2 \sin \theta}, \quad (2)$$

$$v_1(y_1, t) = -\frac{u_1(y_1, t) + u_2(y_1, t)}{2 \cos \theta}. \quad (3)$$

To obtain the horizontal and vertical velocity profiles of (u, v) along the y axis at $x = x_1$, we proposed a time correction method of velocity distributions using a front velocity U_f (Nomura et al., 2018, 2019). This interpolation is applicable in the case that the turbulence statistics are conserved in the measurement region. The details of U_f are described in section 3.1. The turbidity current progresses with almost constant U_f in the case of high-volume release (the initial volume of the heavier fluids is relatively similar to that of the ambient fluid). On the basis of this concept, Eqs. (2) and (3) are modified as follows:

$$u(y, t) = \frac{u_1(y, t - \Delta t) - u_2(y, t + \Delta t)}{2 \sin \theta} \quad (4)$$

$$v(y, t) = -\frac{u_1(y, t - \Delta t) + u_2(y, t + \Delta t)}{2 \cos \theta} \quad (5)$$

where

$$\Delta t = \frac{(y - y_1) \tan \theta}{U_f}. \quad (6)$$

Here, the interpolation quantity is varied due to y . The UVP measurement parameters (Takeda 2012) are presented in Table 1. From the UVP parameters applied in this experiment, the resolution in the vertical direction and the temporal resolution are 0.67 mm and 50 ms, respectively. As the velocity resolution of UVP was 1.399 mm/s and the UVP inclination was 25° , the vertical and horizontal velocity resolutions were $1.399/(\sin 25) = 3.31 \text{ mm/s}$ and $1.399/(\cos 25) = 1.54 \text{ mm/s}$, respectively. There is inevitably some inaccuracy in resolving the turbulence, due to the non-uniformity of turbulence structures during the time between crossing the two separate beams (Eq. (6)), which was estimated to be negligibly small in this experimental setup.

Since d_{50} (12.2 μm) is less than one-tenth of the wavelength of the ultrasound echo of 4 MHz frequency in water (0.74 mm; Table 1), Rayleigh scattering, which is almost isotropic scattering, is generated. In ordinary UVP measurements, the adequate diameter of the tracer particles acting as reflectors of the ultrasound wave is appropriately quarter to half of the wavelength. Hitomi et al. (2018) evaluated whether velocity measurement can be performed correctly using the same particles as in this study and a 4-MHz transducer. They confirmed that the equipment can capture the correct velocity profile for volume fractions of 0.01%–5.00% by comparison with measurements obtained using tracer particles of adequate size.

2.3. Particle Concentration Profile

Ultrasound echo amplitude distributions scattered by suspended particles provide useful information on the particle concentration (e.g. Lee and Hanes, 1995; Thorne and Hanes, 2002; Hurther et al., 2011; Pedocchi and García, 2012). Simmons et al. (2020) applied the technique to observe turbidity currents in a natural environment. Under Rayleigh scattering conditions, Thorne and Hanes (2002) suggested the relationship between the mean-square amplitude of the echo signal $\langle V^2 \rangle$ received by ultrasound transducers and the mass concentration M in kg/m^3 at η , the distance from the transducer, to be:

$$M(\eta) = \langle V^2 \rangle \left(\frac{\psi \eta}{K_s K_t} \right)^2 e^{4\alpha_w \eta} = \langle V^2 \rangle \left(\frac{\psi \eta}{K_s K_t} \right)^2 e^{4(\alpha_w \eta + \int_0^\eta \xi M(\eta) d\eta)} \quad (7)$$

where ψ is the spreading effect of acoustic waves in the near field of a transducer and α_w is the attenuation constant in clear water presented as a function of the temperature, as follows (Fisher and Simmons, 1977):

$$\alpha_w = 10^{-15} (55.9 - 2.37T + 4.477 \times 10^{-2}T^2 - 3.48 \times 10^{-4}T^3) F^2 \quad (8)$$

where T is temperature ($^\circ\text{C}$) and F is the acoustic frequency (Hz). The sediment attenuation constant ξ can then be written as

$$\xi = \frac{3}{4a_s \rho_p} \chi \quad (9)$$

where a_s is the acoustic attenuation constant. χ is the normalized total scattering cross-section (Thorne and Hanes, 2002), represented as

$$\chi = \frac{1.1 \cdot \frac{4}{3} \cdot 0.18 (ka_s)^4}{1 + 1.3 (ka_s)^2 + \frac{4}{3} \cdot 0.18 (ka_s)^4} \quad (10)$$

where k is the wave number of the acoustic wave in water, K_s is a function of the scattering properties of the suspended sediment, and K_t is a constant for the ultrasound system. Pedocchi and García (2012) applied this theory to the echo distributions obtained by UVP, where the echo signal is the result of the acoustic Doppler conversion for velocity profiling. In the UVP Duo, the echo signals are represented as voltage variations with 14 bits within the range ± 2.5 V (8191 = 2.5 V; $-8191 = -2.5$ V). The device adopts time-variable gain values to amplify the echo signal by linear absolute gain with start G_s and end G_e . According to the technical manual for the device, the actual echo intensity V recorded as an electric voltage is derived as

$$V = \frac{V_{amp}}{G_s} \left(\frac{G_s}{G_e} \right)^{\frac{\eta - \eta_s}{\eta_e - \eta_s}} \quad (11)$$

where V_{amp} is the amplified echo signal, and η_s and η_e are the minimum and maximum measurable distance from the transducer, respectively. The detailed characteristics of amplification by UVP Duo are summarized in Table 2.

Table 2

Gain factors to amplify UVP echo signals (courtesy of Met Flow Corp.).

Gain factor G_s / G_e	Basic frequency of ultrasound transducer 4.0 [MHz]
3	0.91
4	1.76
5	3.41
6	6.67
7	15.00
8	25.00
9	60.00

Because of non-linearity in the original form of Eq. (7), the solution for M must be acquired by iterative analysis, whereas Lee and Hanes (1995) proposed an explicit form by introducing the concentration at an initial point M_I by differentiating the logarithm of Eq. (7) with respect to η as follows:

$$\frac{dM(\eta)}{d\eta} - \left(2 \frac{\eta \frac{d\sqrt{\langle V^2 \rangle}}{d\eta} + \sqrt{\langle V^2 \rangle}}{\eta \sqrt{\langle V^2 \rangle}} + 4\alpha_w \right) M(\eta) = 4\xi M(\eta)^2 \quad (12)$$

where $\psi(\eta)$ in Eq. (7) is assumed to be a constant for the case of measurements in the far field of an ultrasound wave (Downing et al., 1995), and disappears by the differentiation in Eq. (12), as do K_s and K_t . According to the general solution of Bernoulli differential equations, the analytical solution of Eq. (12) can be presented as

$$M(\eta) = \frac{\langle V^2 \rangle \eta^2 e^{4\alpha_w \eta}}{C - 4\xi \int \langle V^2 \rangle \eta^2 e^{4\alpha_w \eta} d\eta} \quad (13)$$

where, C denotes the integral constant.

A boundary condition is required to determine C in Eq. (13). Here we assume that the heavier fluid intruding into the ambient fluid as a turbidity current maintains its initial concentration close to the bed. This condition is reasonably applicable, according to previous reports by Felix et al. (2005) and Theiler and Franca (2016). The boundary condition, $M_B = 1008 \text{ kg}/\text{m}^3$ at the bottom and $\eta = \eta_B$, is thus provided, and C is derived as follows:

$$C = \frac{r_B^2 \langle V^2 \rangle_B e^{4\alpha_w r_B}}{M_B} + 4\xi \int_{r_i}^{r_B} r^2 \langle V^2 \rangle e^{4\alpha_w r} dr \quad (14)$$

Applying Eq. (14) to Eq. (13), we have:

$$M(r) = \frac{r^2 \langle V^2 \rangle e^{4\alpha_w r}}{\frac{1}{M_B} r_B^2 \langle V^2 \rangle_B e^{4\alpha_w r_B} + 4\xi \int_r^{r_B} r^2 \langle V^2 \rangle e^{4\alpha_w r} dr} \quad (15)$$

By discretizing Eq. (15), we finally obtain

$$M_n = \frac{r_n^2 \langle V^2 \rangle_n e^{4\alpha_w r_n}}{\left[\frac{1}{M_B} r_B^2 \langle V^2 \rangle_B e^{4\alpha_w r_B} + 4\Delta r \xi \sum_{i=n+1}^N (r_i^2 \langle V^2 \rangle_i e^{4\alpha_w r_i} + r_{i-1}^2 \langle V^2 \rangle_{i-1} e^{4\alpha_w r_{i-1}}) \right]} \quad (16)$$

where n represents the order of measurement (i.e. i -th) points from the transducer.

3. Results

3.1. Front Advection Velocity

Images extracted every 1.5 s from 16.5 s after opening of the gate are shown in Fig. 4. The movie was taken with a digital camera (Nikon D5500) from the side window of the flume at 20 frames per second. The shooting area is around x_1 in Fig. 1. The frame rate was purposely set to be the same as the profile sampling rate of the UVP (temporal resolution 50 ms).

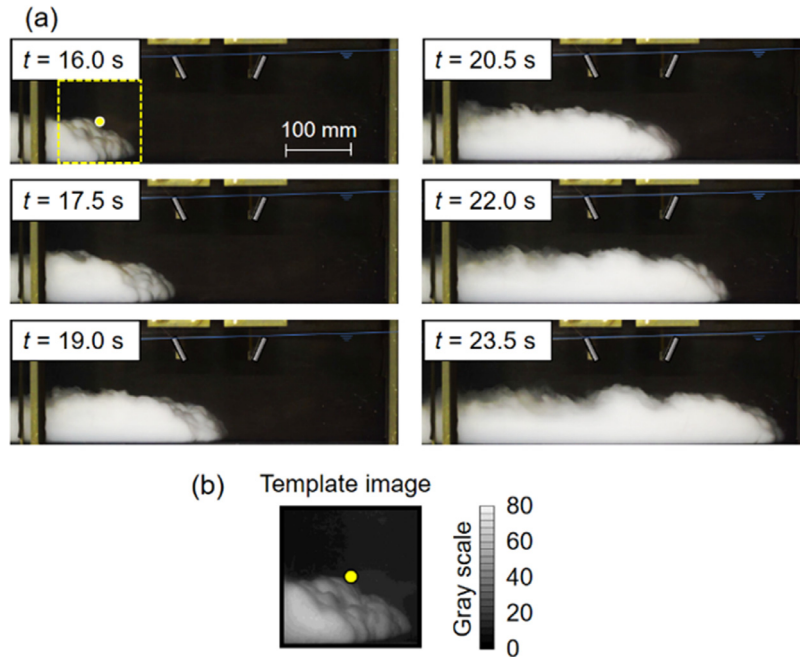


Fig. 4. (a) Snapshots of the experimental turbidity current from $t = 16.0$ to 23.5 s and (b) the template image that was used for correlation with other images to measure the front velocity.

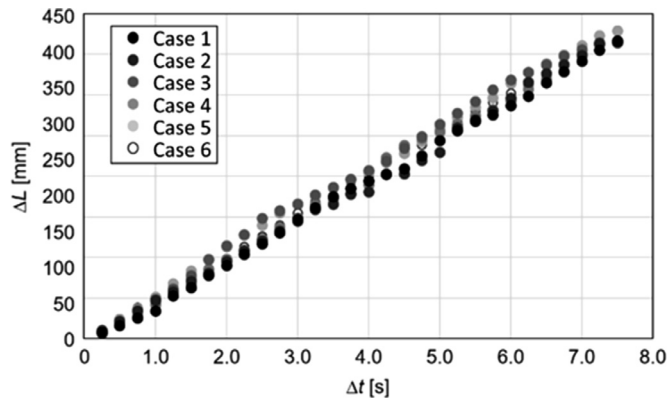


Fig. 5. Temporal evolution of the location of the front of the turbidity current. The abscissa and ordinate indicate the elapsed time Δt from $t = 16$ s and the displacement of the detected head position from the initial position, respectively.

In the images obtained, unsteady interfaces were observed from the front edge to the upper boundary with the ambient water. This finding is in agreement with the observations of [Simpson and Britter \(1979\)](#). To measure the front velocity U_f , pattern matching was applied to the sequential images. A template image with 451×451 pixels was prepared from the image at $t = 16$ s ([Fig. 4\(b\)](#)), and the corresponding head position of the turbidity current was determined every 250 ms by computing the image correlation between the template and the visualized images. To confirm reproducibility, the experiments were repeated six times using the same initial and boundary conditions. The head positions with time are shown in [Fig. 5](#). In all cases, similar migration of the head position was observed with small deviation, proving experimental reproducibility of the current.

In [Fig. 5](#), the slope gradient remains constant with time. This result implies a steady state of the current between the gravity-driven hydrostatic force and the flow resistance caused by the counterflow that balances the buoyancy force along the upper boundary of the current. The front velocities U_f of each experimen-

tal run were determined from the slope angle using least squares ([Table 3](#)). The obtained values of U_f are similar; the average value is 50.6 mm/s with small fluctuations of 0.41 mm/s. As turbidity currents are regarded as a type of gravity current, the densimetric Froude number Fr' of the flow and the Reynolds number Re (following [Simpson and Britter, 1979](#); [Kneller et al., 1999](#)) can be calculated as follows:

$$Fr' = \frac{U_f}{\sqrt{g'H}} \quad (17)$$

$$Re = \frac{\rho_H U_f H}{\mu} \quad (18)$$

where H is the height of the heavy fluid and g' is the reduced gravitational acceleration. In the produced currents, the height H converged to a stable value in the downstream region. At the measurement window $x = x_1$, the current height was $H = 79$ mm, giving $Fr' = 0.63$ and $Re = 4.0E3$ in this experiment. These values of the non-dimensional numbers indicate that the flow was fully turbulent and subcritical (e.g. [Kneller et al., 1999](#)).

3.2. Visualization of the Inner Flow

3.2.1. Velocity profile

The spatio-temporal distributions of horizontal and vertical velocities (u and v) of a typical run are shown in [Fig. 6](#). This illustration was produced based on the theory described in [Section 2.2](#) and transformation of the time series into a representation of the 2D flow structure. As shown by the image of the velocity magnitude, u is dominant in the bottom half of the flume; i.e., $y \approx 0-70$ mm. Due to intrusion of the flow, positive v (i.e. upward flow) is observed at $t = 20-25$ s, representing lifting up of the ambient water. As the lock-exchange flume is a closed system, a counter flow of ambient fluid is generated and a negative horizontal velocity is observed at $y \approx 50-70$ mm. As the lower measurement limitation in this system is a particle concentration of 0.01% ([Hitomi et al., 2018](#)), the velocity values above that height are fluctuating and unreliable. The distribution of u describes a

Table 3
Summary of front velocity values computed by pattern matching.

Exp. Number	1	2	3	4	5	6	Ave.	Std. Dev.
U_f [mm/s]	50.0	50.0	50.9	50.6	51.0	50.9	50.6	0.41

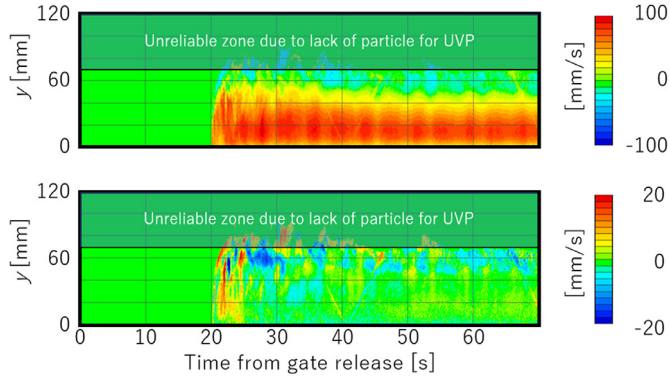


Fig. 6. Spatio-temporal distribution of the horizontal (upper illustration) and vertical (lower illustration) velocity components. y = height above the bed. Measurement data above $y = 70$ mm are unreliable due to the lack of particles.

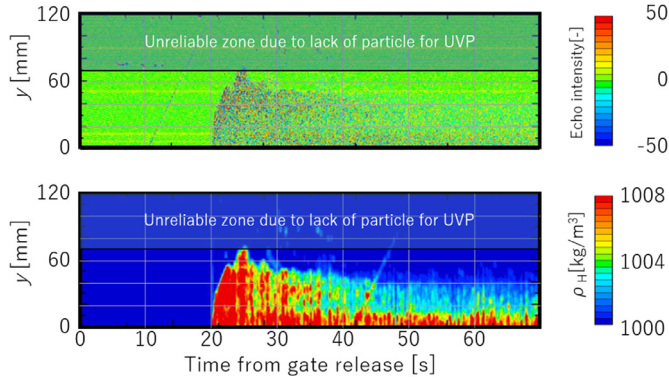


Fig. 7. Spatio-temporal distribution of the backscatter echo intensity (upper illustration) and bulk density of the particle-suspended fluid computed from echo intensity (lower illustration). Measurement data above $y = 70$ mm are unreliable due to the lack of particles.

quasi-periodic fluctuation in the main body of the current with time. This fluctuation can be attributed to the vortex structures emerging near the upper boundary of the current, which are also observed in the vertical velocity v .

3.2.2. Concentration profile

The concentration profile of quartz particles was obtained from the spatio-temporal echo distribution measured by UVP by means of the algorithm explained in Section 2.3. To reduce the influence of measurement noise on the echo, the mean-square amplitude of the echo signal $\langle V^2 \rangle$ was calculated from 5×5 measurement points, yielding an equivalent resolution of $3.4 \text{ mm} \times 0.25 \text{ s}$ in the space-time domain as follows:

$$\langle V^2 \rangle_{i,j} = \frac{1}{5 \times 5} \sum_{\Delta i=-2}^2 \sum_{\Delta j=-2}^2 [V^2(i + \Delta i, j + \Delta j)] \quad (19)$$

where i and j represent discrete coordinates in time and space, respectively.

The spatio-temporal density distribution of the quartz suspension calculated using Eq. (1) and the measured values are depicted in Fig. 7. The head region of the current has a high density of almost 1008 kg/m^3 , corresponding to the initial density of the heav-

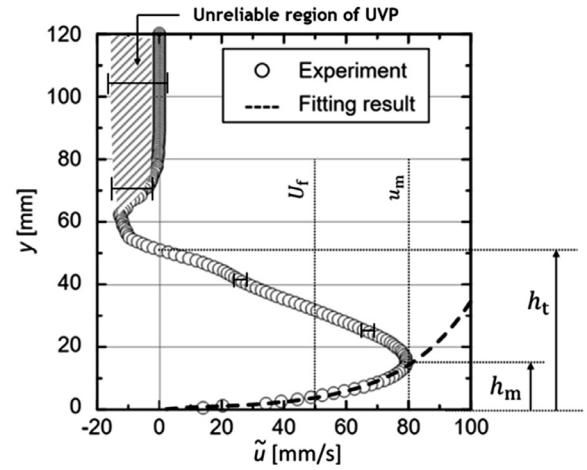


Fig. 8. Time-averaged distribution of the horizontal velocity component (\tilde{u}) in the body region for $35 < t < 70$ s. The hatched area indicates the region for which the data are unreliable due to the lack of particles for UVP measurement. The heights h_t and h_m are defined as the positions at zero-cross velocity and maximum velocity, respectively. The error bars indicate 95% confidence interval of the sample mean for the horizontal velocity in the sampled period, which becomes large at $y > 70$ mm due to lack of particles necessary for UVP measurement.

ier fluid, consistent with the findings of Felix et al. (2005). This result supports the hypothesis that the turbidity current lifts up particles in the front part of the current to raise its own potential energy. In addition, particles are fed to the front bottom part from the lower high-density layer that slides from upstream; this process is visible as vertical stepwise stratification in Fig. 7. The combination of these structures in a turbidity current is consistent with previous reports (e.g. Pantin, 1979; Parker et al., 1986; McCaffrey et al., 2003; Pantin and Franklin, 2011); i.e., uplifting of heavier fluid at the front and re-supply of the density difference between the main body of the current and the ambient fluid (Nomura et al., 2019).

3.3. Data Analysis and Discussion

3.3.1. Velocity and Concentration Profiles of the Body Region

This section focuses on the body region, which is recognized as a local quasi-steady flow behind the head (Kneller and Buckee, 2000 and references therein). Previous studies provide no clear criteria to distinguish the head and body regions, because they observed mainly the outline of the sediment layer. We focused on the distribution of v to define the beginning of the body region and concluded that this region arrives by $t = 35$ s, because the influence of the uplifted flow of the head region disappears after $t \approx 35$ s in Fig. 6. Fig. 8 shows the profile of the mean horizontal velocity (\tilde{u}) in the body averaged for 35 s after $t = 35$ s. The profile shows the zero-crossing point on the y axis at $y = h_t = 50$ mm, which corresponds to the thickness of the current defined by velocity. The maximum velocity $u_m = 80$ mm/s is observed at $y = h_m = 14$ mm, which is located in the lower half of the current (i.e. $h_m < h_t/2$). This velocity is 1.6 times as high as the front velocity U_f ; this difference results in recirculation of the flow within the body region. Outside the current at $y > h_t$, a layer of reverse flow takes place as a counter flow.

Table 4
Summary of computed values of the friction velocity and the zero-velocity roughness height.

Exp. Number	1	2	3	4	5	6	Ave.	Std. Dev.
u^* [mm/s]	9.2	11.8	12.8	12.3	11.1	10.8	11.3	1.2
y_0 [mm]	0.404	0.925	0.948	0.825	0.725	1.110	0.820	0.220

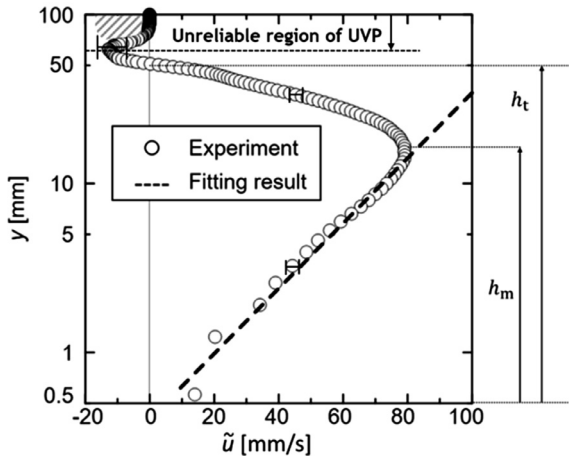


Fig. 9. Fitting result with log-law profile (Eq. (20)) for the averaged horizontal velocity profile (\tilde{u}) in the lower shear layer of the body region for $35 < t < 70$ s. The error bars indicate the confidence interval the same as in Fig. 8.

Altınakar et al. (1996) reported that the profile of \tilde{u} is similar in shape to that of a jet flow parallel to a wall consisting of two vertical regions: a wall region ($y < h_m$) and a free jet region ($h_m < y < h_t$). They suggested a model fitting for the wall region with a logarithmic profile of turbulent boundary layers:

$$\tilde{u}(y) = \frac{u^*}{\kappa} \ln \frac{y}{y_0} \quad (20)$$

where u^* and y_0 denote the friction velocity and the zero-velocity roughness height, respectively. Assuming a smooth bed condition (e.g. Zordan et al., 2018), substitution of the von Karman constant $\kappa = 0.41$ in Eq. (20) yields the values presented in Table 4 for six runs of the same current. The average values are $u^* = 11.3$ mm/s and $y_0 = 0.82$ mm. The value y_0 is larger than the expected value for the smooth floor of the flume, implying a rough wall effect resulting from particle deposition on the floor. The logarithmic velocity profile with these constants is indicated by the broken line in Fig. 8 on a normal scale and Fig. 9 on a semi-logarithmic scale; the fitting curve seems to represent the experimental data reasonably for $y < h_m$.

The time-averaged distribution of the normalized particle concentration $\bar{C} [\%] = (\rho_f - \rho_L)/(\rho_H - \rho_L) \times 100$ from M for 35 s after $t = 35$ s is shown in Fig. 10. The value decreases monotonically with respect to y from the maximum concentration at the bottom, and approaches zero at $y = h_t$. The solid curve in Fig. 10 shows \tilde{u} , which is also illustrated in Fig. 8. These vertical gradients (Fig. 11) reveal a more precise structure, which appears to exhibit multiple steps in the concentration profile. The profile of C has three major inflection points that divide the whole structure into four layers: the wall shear layer at $0 < y < h_m$; the second layer at $h_m < y < h_s = 25$ mm; the third layer at $h_s < y < h_t$; and the outer region at $y > h_t$. As is visible in the profile of \tilde{u} , the second and third layers exhibit a negative velocity gradient ($d\tilde{u}/dy < 0$). This result implies that particle diffusion takes place non-analogously due to momentum diffusion inside these layers. The details of the mechanism are discussed in Section 4.2.

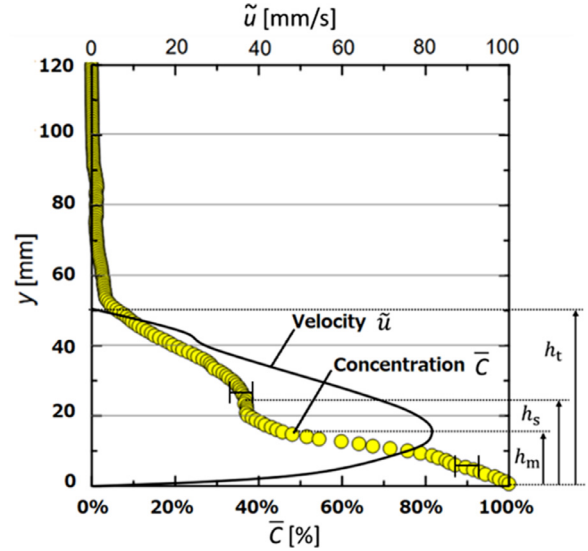


Fig. 10. Time-averaged profiles of particle concentration (\bar{C}) in the body region for $35 < t < 70$ s, relative to the time-averaged velocity profile. The error bar for particle concentration is estimated from the r.m.s. of temporal fluctuations in echo intensity, V_{rms} , reflecting to variation of C in Eq. (14).

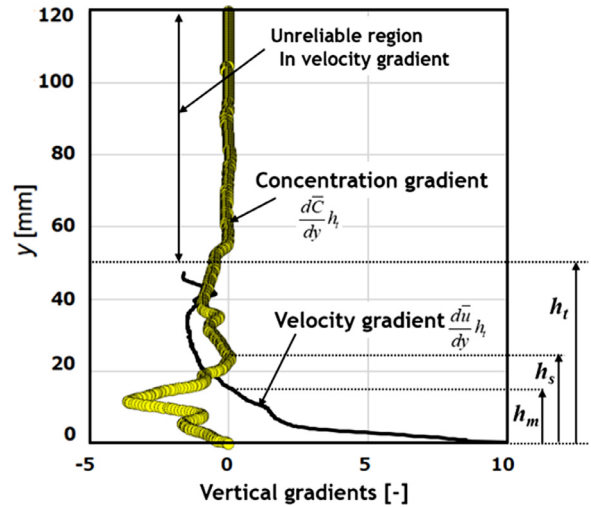


Fig. 11. Time-averaged vertical gradients in particle concentration and horizontal flow velocity in the body region for $35 < t < 70$ s. The velocity gradient is computable only at $h < h_t$.

3.4. Momentum Conservation Law for the Body Region

To discuss the shear stress profile in the body region, we incorporate two-fluid model equations that are local volume-averaged descriptions of the momentum conservation equation for two phases:

$$\frac{\partial f_L \rho_L \mathbf{u}_L}{\partial t} + \nabla \cdot f_L \rho_L \mathbf{u}_L \mathbf{u}_L = -f_L \nabla p + \mathbf{M}_{LL} + \mathbf{M}_{SL} \quad (21)$$

$$\frac{\partial f_S \rho_S \mathbf{u}_S}{\partial t} + \nabla \cdot f_S \rho_S \mathbf{u}_S \mathbf{u}_S = -f_S \nabla p + \mathbf{M}_{SS} + \mathbf{M}_{LS} \quad (22)$$

where the subscripts L and S denote liquid and solid phases, respectively. The primitive variables f , \mathbf{u} , and p are the volume fraction, velocity vector, and pressure, respectively, as local volume-averaged quantities. The terms \mathbf{M}_{LL} and \mathbf{M}_{SS} represent the inner phase momentum transport (e.g. Murai and Matsumoto, 2000), which is modeled in the case of particle-laden flow as follows:

$$\begin{aligned} & \mathbf{M}_{LL} + \mathbf{M}_{SS} \\ &= \nabla \cdot \mu_L \left\{ \nabla \mathbf{u}_L + (\nabla \mathbf{u}_L)^T - \frac{2}{3} (\nabla \cdot \mathbf{u}_L) \right\} + f_L \rho_L \mathbf{g} \\ &+ \nabla \cdot \mu_S \left\{ \nabla \mathbf{u}_S + (\nabla \mathbf{u}_S)^T - \frac{2}{3} (\nabla \cdot \mathbf{u}_S) \right\} + f_S \rho_S \mathbf{g} \end{aligned} \quad (23)$$

where μ and \mathbf{g} are the viscosity and the acceleration due to gravity, respectively. The slip velocity between \mathbf{u}_L and \mathbf{u}_S can be estimated by the following equation for the Stokes number:

$$St = \frac{\rho_p d_p^2 U_0}{18 \mu_w L_0} \quad (24)$$

where U_0 and L_0 are the characteristic velocity and length, represented by the time-averaged values of the layer-averaged velocity \bar{u} and the thickness of the current h_t . This equation yields St values on the order of $10^{-5} \ll 1$, which proves that the phases have a common fluid velocity field $\mathbf{u}_L = \mathbf{u}_S = \mathbf{u}$. Hence, Eq. (16) can be rewritten as

$$\mathbf{M}_{LL} + \mathbf{M}_{SS} = \nabla \cdot \mu_H \left\{ \nabla \mathbf{u} + (\nabla \mathbf{u})^T - \frac{2}{3} (\nabla \cdot \mathbf{u}) \right\} + f_L \rho_L \mathbf{g} + f_S \rho_S \mathbf{g} \quad (25)$$

where μ_H is the effective viscosity of a particle-suspended fluid, which was empirically modeled by Davidson et al. (1977) as follows:

$$\mu_H = \mu_w (1 - 1.35 f_S)^{-2.5} \quad (26)$$

\mathbf{M}_{SL} and \mathbf{M}_{LS} in Eqs. (21) and (22) represent mutual phase momentum transfers and satisfy the following relation due to Newton's third law (regarding action and reaction):

$$\mathbf{M}_{SL} + \mathbf{M}_{LS} = 0. \quad (27)$$

Taking the sum of Eqs. (21) and (22), the total momentum conservation equation in terms of total mass can be described as

$$\begin{aligned} & \frac{\partial (f_L \rho_L + f_S \rho_S) \mathbf{u}}{\partial t} + \nabla \cdot (f_L \rho_L + f_S \rho_S) \mathbf{u} \mathbf{u} = -(f_L + f_S) \nabla p \\ &+ \nabla \cdot \mu_H \left\{ \nabla \mathbf{u} + (\nabla \mathbf{u})^T - \frac{2}{3} (\nabla \cdot \mathbf{u}) \right\} + (f_L \rho_L + f_S \rho_S) \mathbf{g} \end{aligned} \quad (28)$$

For mass conservation, the following relations apply to the present incompressible particle-laden flow:

$$f_L + f_S = 1 \quad (29)$$

$$f_L \rho_L + f_S \rho_S = \rho_H \quad (30)$$

Rewriting Eq. (28) to incorporate Eqs. (29) and (30), we obtain

$$\frac{\partial \rho_H \mathbf{u}}{\partial t} + \nabla \cdot \rho_H \mathbf{u} \mathbf{u} = -\nabla p + \nabla \cdot \mu_H \left\{ \nabla \mathbf{u} + (\nabla \mathbf{u})^T - \frac{2}{3} (\nabla \cdot \mathbf{u}) \right\} + \rho_H \mathbf{g}. \quad (31)$$

For an incompressible divergence-free fluid velocity vector field, Eq. (31) can be further simplified as

$$\frac{\partial \rho_H \mathbf{u}}{\partial t} + \nabla \cdot \rho_H \mathbf{u} \mathbf{u} = -\nabla p + \nabla^2 (\mu_H \mathbf{u}) + \rho_H \mathbf{g}. \quad (32)$$

Finally, the horizontal component of Eq. (32), which dominates the turbidity current in the body region, is described as follows:

$$\begin{aligned} & \frac{\partial \rho_H u}{\partial t} + \frac{\partial \rho_H u u}{\partial x} + \frac{\partial \rho_H u v}{\partial y} + \frac{\partial \rho_H u w}{\partial z} \\ &= -\frac{\partial p}{\partial x} + \left(\frac{\partial^2 \mu_H u}{\partial x^2} + \frac{\partial^2 \mu_H u}{\partial y^2} + \frac{\partial^2 \mu_H u}{\partial z^2} \right) + F_g \end{aligned} \quad (33)$$

where w is the spanwise velocity. F_g denotes the external force due to gravity.

3.5. Shear Stress Components

We separate the primitive variables into time-average and fluctuation components (analogous to Reynolds decomposition for two-phase flow; e.g., Murai et al., 2006) in the following manner:

$$\rho_H = \bar{\rho}_H + \rho'_H \quad (34)$$

$$u = \bar{u} + u'$$

$$v = \bar{v} + v'$$

$$w = \bar{w} + w'$$

$$\mu_H = \bar{\mu}_H + \mu'_H$$

Substituting these values into Eq. (33), an equation describing the shear stress balance is obtained:

$$\begin{aligned} & \frac{\partial}{\partial x} (\bar{\rho}_H \bar{u} \bar{u} + \overline{\rho'_H u' u'} + 2 \overline{\rho'_H u' \bar{u}} + \overline{\rho'_H u' u'}) \\ &+ \frac{\partial}{\partial y} (\bar{\rho}_H \bar{u} \bar{v} + \overline{\rho'_H u' v'} + \rho'_H u' \bar{v} + \overline{\rho'_H u' v'}) \\ &+ \frac{\partial}{\partial z} (\bar{\rho}_H \bar{u} \bar{w} + \overline{\rho'_H u' w'} + \rho'_H u' \bar{w} + \overline{\rho'_H u' w'}) \\ &= \frac{\partial^2 (\bar{\mu}_H \bar{u} + \overline{\mu'_H u'})}{\partial x^2} + \frac{\partial^2 (\bar{\mu}_H \bar{u} + \overline{\mu'_H u'})}{\partial y^2} + \frac{\partial^2 (\bar{\mu}_H \bar{u} + \overline{\mu'_H u'})}{\partial z^2} - \frac{\partial p}{\partial x} + F_g. \end{aligned} \quad (35)$$

In the body region, there is no mean current other than the horizontal current to apply $\bar{v} = \bar{w} = 0$ in Eq. (35) and the gradient of the momentum in the streamwise and spanwise directions is negligible; consequently, we have

$$\frac{\partial}{\partial y} (\overline{\rho'_H u' v'} + \overline{\rho'_H v' \bar{u}} + \overline{\rho'_H u' v'}) = \frac{\partial^2 (\bar{\mu}_H \bar{u} + \overline{\mu'_H u'})}{\partial y^2} + \frac{\partial p}{\partial x} + F_g. \quad (36)$$

Eq. (36) is rewritten to explicitly show the terms balancing with the streamwise pressure gradient:

$$\begin{aligned} & \frac{\partial p}{\partial x} \\ &= \frac{\partial}{\partial y} \left(\frac{\partial \bar{\mu}_H \bar{u}}{\partial y} + \frac{\partial \overline{\mu'_H u'}}{\partial y} - \overline{\rho'_H u' v'} - \overline{\rho'_H v' \bar{u}} - \overline{\rho'_H u' v'} \right) + F_g. \end{aligned} \quad (37)$$

Consequently, we extract five components that comprise the shear stress profile inside the turbidity current as follows:

$$\tau_1 = \frac{\partial \bar{\mu}_H \bar{u}}{\partial y} \text{ (viscous shear stress)}, \quad (38)$$

$$\tau_2 = \frac{\partial \overline{\mu'_H u'}}{\partial y}, \quad (39)$$

$$\tau_3 = -\overline{\rho'_H u' v'} \text{ (Reynolds shear stress)}, \quad (40)$$

$$\tau_4 = -\overline{\rho'_H v' \bar{u}}, \quad (41)$$

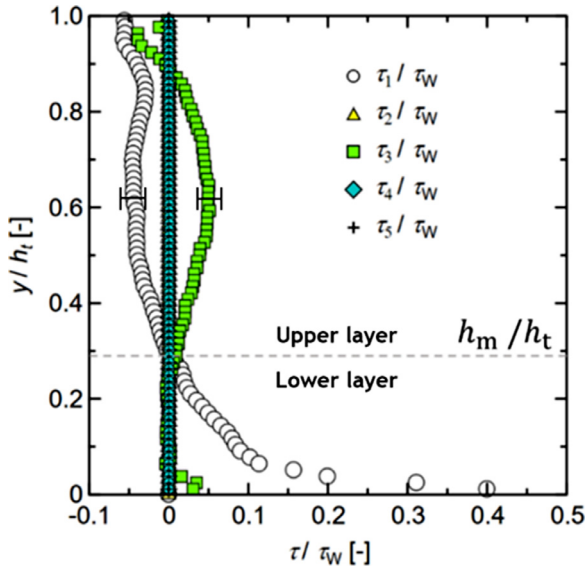


Fig. 12. Shear stress distributions computed from UVP measurements, dominated by the viscous shear stress τ_1 and Reynolds shear stress τ_3 . The symbols for τ_2 , τ_4 , and τ_5 overlap; the values of these parameters are less than 1% of the wall shear stress. Error bars are estimated from the spatial resolution of UVP. Error bars indicate the 95% confidence interval of the sample mean for measured local stress.

$$\tau_5 = -\overline{\rho'_H u'v'} \quad (42)$$

Note that the term F_g in Eq. (37) is negligible, because the current is driven by a horizontal pressure gradient caused by differences in hydrostatic pressure between the far upstream and far downstream parts of the body region.

3.6. Shear Stress Characteristics

The computed results of the five components of shear stress are shown in Fig. 12. The ordinate denotes the height from the bed normalized by h_t and the abscissa plots the shear stress normalized by the wall shear stress τ_W . The wall shear stress is computed from the formula for friction velocity u^* :

$$\tau_W = \rho_H u_*^2 \quad (43)$$

The estimated wall shear stress τ_W is 0.086 Pa. The broken line in Fig. 12 indicates the position of $h_m/h_t = 0.28$, which separates the lower and upper shear layers of the turbidity current. The results demonstrate that the viscous shear stress τ_1 and the Reynolds shear stress τ_3 govern the whole structure. Furthermore, these two parameters take opposite values above h_m , implying balancing of the shear stress in the upper shear layer. In the lower layer, only the viscous shear stress τ_1 dominates, except near the flume bottom. This indicates significant suppression of the Reynolds shear stress τ_3 , which is attributed to relaminarization caused by a high density of particles smaller than one-tenth of the estimated integral scale of turbulence (Gore and Crowe, 1989; Crowe et al., 1996). Cossu and Wells (2012) also found relaxation of Reynolds shear stress in the lower layer as a result of particles. Their particles were 30 μm in mean diameter, whereas ours are 10 μm diameter. This size difference reduced the particle settling velocity in our experiments to $(10/30)^2 = 1/9$ times that of Cossu and Wells (2012), resulting in further effective relaminarization in our experiments. In contrast, the rest of the stress terms, τ_2 , τ_4 , and τ_5 , are almost zero, meaning that the turbidity current is less affected by coupling of velocity fluctuation with local fluid properties; i.e., density and effective viscosity fluctuations ($\overline{\mu'_H}$ and $\overline{\rho'_H}$).

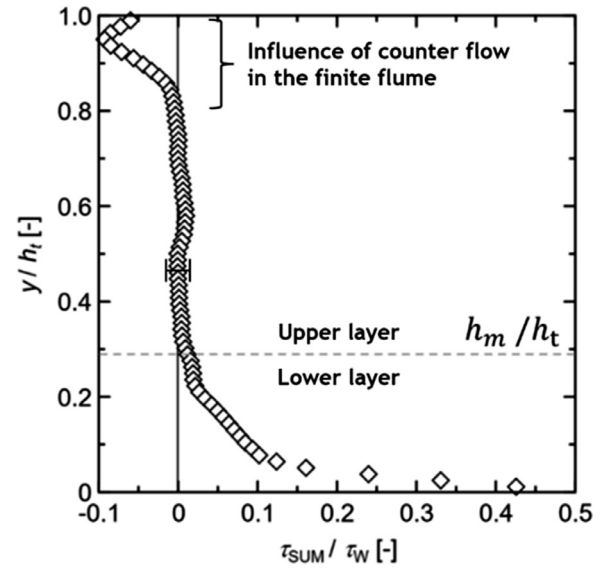


Fig. 13. Distribution of the sum of five shear stress components, showing significant shear stress relaxation in the upper layer at $y > h_m$. Error bars indicate the 95% confidence interval the same as in Fig. 12.

The total shear stress profile calculated by taking the sum of the five stress values is depicted in Fig. 13. Due to the mutual balancing of τ_1 and τ_3 , the shear stress disappears in the range $0.3 < y/h_t < 0.8$. The friction characteristics are mostly determined by the lowest layer of the current at $y/h_t < 0.2$, which balances the streamwise pressure gradient.

A small negative total stress may be present close to the border of the current at $y/h_t > 0.8$, where we observed slow density propagation against the main stream due to a counter flow. This negative total stress is derived from an effect of the counter flow induced in the finite flume used in our experiments, and is not discussed further in this paper.

A key finding from the present study is the fact that the layer at $0.3 < y/h_t < 0.8$ induces a positive Reynolds shear against the negative mean velocity gradient. This result is consistent with the observations of Kneller et al. (1999). This effect means that negative momentum transfer can occur in a density-stratified medium; i.e. density increases with depth in the fluid with shear (Kneller et al., 2016; Sequeiros et al., 2010). In thermal stratification of single-phase flow, Komori et al. (1983), Piccirillo and van Atta (1997), and Nagata and Komori (2001) found similar negative momentum transfer. According to Komori et al. (1983), such an inverse-gradient diffusion can be explained by a density wave overshadowing shear-induced waves at a frequency lower than

$$f_r = \sqrt{\frac{g}{\rho_W} \cdot \frac{\rho_H - \rho_W}{h_t}} \simeq 1.25 \text{ Hz} \quad (44)$$

Here, $f_r = 1.25$ Hz is the estimated frequency under the present conditions. As most of the turbulence scales in our case satisfy $f_r < 1.25$ Hz (see v -component in Fig. 6), analogy to the turbulence in thermal stratification is inferred. In shear flows, the following Richardson number describes the stability of the density stratification:

$$Ri = \frac{g}{\rho_W} \frac{\partial \rho / \partial y}{(\partial \bar{u} / \partial y)^2} \simeq \frac{\Delta \rho}{\rho_W} \frac{g(h_t - h_m)}{u_m^2} = 0.008 \frac{9.8 \cdot 0.035}{0.08^2} = 0.6 \sim O(1) \quad (45)$$

In the present experiment, Ri takes $O(1)$ in the upper shear layer, meaning that Richardson waves interact with turbulent shear. A similar conclusion was obtained by Stacey and

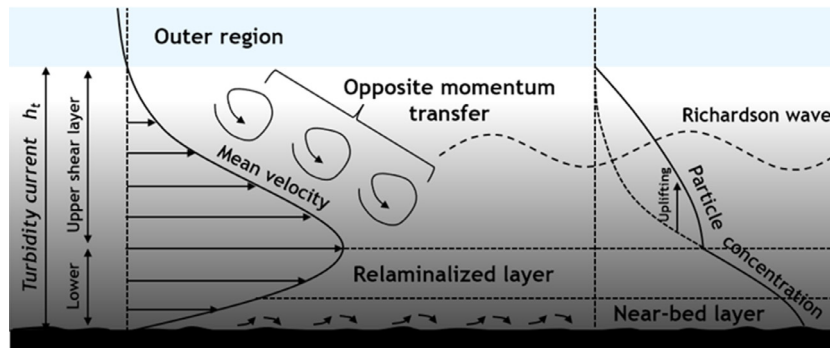


Fig. 14. Schematic diagram of the flow structure inferred from the present experimental results.

Bowen (1988), Kneller et al. (1997), and Sequeiros et al. (2010) for density destratification caused by shear. Dorrell et al. (2019) found the emergence of an anti-frictional layer that sharpened a gravity current. In their explanation based on a real long-distance current measured on the sea floor, the density gradient enhanced negative turbulent momentum transfer to form a jet-like stream as the flow moved downstream. Our flume experiment yielded analogous results to that study at a point in a slowly developing turbidity current.

A summary of the present findings for the body region is illustrated in Fig. 14. According to the simultaneous measurement of flow velocity and particle concentration profiles, the body region consists of four layers: the near-bed layer, the lower shear layer, the upper shear layer, and the outer region. In the near-bed layer, there is a high particle concentration with spatial fluctuations, which acts as a rough wall. This roughness induces local Reynolds shear stress to have a turbulent frictional stress on the wall. The lower layer, which is between the near-bed layer and the maximum flow velocity height, maintains a laminar-like quasi-steady state with relatively minor turbulence. This behavior is attributed to relaminarization of turbulence caused by the particles being much smaller than the integral scale of turbulence. In the upper shear layer, Reynolds shear stress takes the opposite sign to the viscous shear stress, canceling out the total shear stress. This result could be explained by the excitation of a Richardson wave in the vertical density gradient field with shear because the elliptic fluid motion of the wave enhances backward momentum transfer from lower- to higher-velocity regions (counter-clockwise rotation in Fig. 14). Dorrell et al. (2019) suggested an analogous mechanism for a turbidity current in nature, and this proposal is verified by the shear stress profiles obtained from the present laboratory flume experiments.

4. Conclusions

Turbidity currents reproduced in a laboratory flume were visualized by means of UVP that was extended to capture 2D velocity and particle concentration profiles. Subsequently, we focused on the inner flow structures of the body of the current, in which the mechanism of reduced flow resistance was revealed. On the basis of the results, we obtained the following conclusions.

- (1) We successfully explored the internal two-phase flow structure of the optically inaccessible turbidity current by means of UVP. The use of two measurement lines for ultrasound Doppler signals enabled simultaneous measurement of both horizontal and vertical velocity components. Ultrasound echo amplitude was used to detect the particle concentration as a function of time together with velocity measurement. The combined information for all three components was used to reconstruct the

two-phase flow field of the current. In the head region, we observed a rapid ascending flow that lifted up the particle-laden suspension supplied from the bottom layer. In the main body region, the current could be divided into layers on the basis of the measured velocity and concentration distribution. The particle concentration exhibited steep stratification in the bottom layer, stepwise stratification in the upper shear layer, and convergence to zero in the outer layer.

- (2) From two-fluid model equations for particulate two-phase flows, five kinds of two-phase turbulent shear stress were extracted. Substituting the data obtained by UVP, the internal flow resistance inside the body region was quantitatively assessed. We detected two features of the current from the analysis. One feature is negative momentum transfer against the mean shear that is induced in the upper shear layer and associated with a Richardson wave; i.e., the shear rate and the density wave interact to enhance the sharpening of the flow velocity profile. This result supports the mechanism observed in nature reported by Dorrell et al. (2019). The other feature is suppression of turbulence in the lower shear layer, where only viscous stress dominates the flow resistance except in the near-bed layer that is influenced by particle deposition. Both features explain the reduction of flow resistance within the body region of the turbidity current that is maintained downstream.

Author statement

Jumpei Hitomi: Conceptualization, Methodology, Investigation, Writing- Original draft preparation

Shun Nomura: Conceptualization, Methodology, Investigation, Data curation, Writing- Original draft preparation, Writing- Reviewing and Editing

Yuichi Murai: Visualization, Investigation, Writing- Original draft preparation, Writing- Reviewing and Editing

Giovanni De Cesare: Conceptualization, Methodology, English proofreading, Supervision

Yuji Tasaka: Data analysis, Visualization, Writing- Original draft preparation, Writing- Reviewing and Editing.

Yasushi Takeda: Conceptualization, Supervision

Hyun Jin Park: Data analysis, Visualization, Writing- Original draft preparation, Writing- Reviewing and Editing.

Hide Sakaguchi: Conceptualization, Supervision

Declaration of Competing Interest

The authors whose name are listed immediately below certify that they have NO affiliations with or involvement in any organization or entity with any financial interest (such as honoraria; educational grants; participation in speakers' bureaus; membership, employment, consultancies, stock ownership, or other equity interest;

and expert testimony or patent-licensing arrangements), or non-financial interest (such as personal or professional relationships, affiliations, knowledge or beliefs) in the subject matter or materials discussed in this manuscript.

Acknowledgments

The authors thank Dr. S. Chamoun for her support and helpful comments. This work was supported by the JAMSTEC Researcher Overseas Dispatch Budget and a Grant-in-Aid for Young Scientists [grant number 15K18115] from the Japan Society for the Promotion of Science.

References

- Altinakar, M.S., Graf, W.H., Hopfinger, E.J., 1996. Flow structure in turbidity currents. *J. Hydraul. Res.* 34 (5), 713–718. doi:10.1080/00221689609498467.
- Amy, L.A., Peakall, J., Talling, P.J., 2005. Density- and viscosity-stratified gravity currents: Insight from laboratory experiments and implications for submarine flow deposits. *Sediment Geol.* 179, 5–29. doi:10.1016/j.sedgeo.2005.04.009.
- Azpiroz-Zabala, M., Cartigny, M.J., Talling, P.J., Parsons, D.R., Sumner, E.J., Clare, M.A., Simmons, S.N., Cooper, C., Pope, E.L., 2017. Newly recognized turbidity current structure can explain prolonged flushing of submarine canyons. *Science advances* 3 (10), e1700200. doi:10.1126/sciadv.1700200.
- Baas, J.H., McCaffrey, W.D., Houghton, P.D.W., Choux, C., 2005. Coupling between suspended sediment distribution and turbulence structure in a laboratory turbidity current. *J. Geophys. Res.* 110, C11015. doi:10.1029/2004JC002668.
- Bux, J., Paul, N., Hunter, T.N., Peakall, J., Dodds, J.M., Biggs, S., 2017. In situ characterization of mixing and sedimentation dynamics in an impinging jet ballast tank via acoustic backscatter. *AIChE J.* 63, 2618–2629. doi:10.1002/aic.15683.
- Cenedese, C., Adduce, C., 2008. Mixing in a density driven current flowing down a slope in a rotating fluid. *J. Fluid Mech.* 604, 369–388. doi:10.1017/S0022112008001237.
- Chamoun, S., De Cesare, G., Schleiss, A.J., 2016. Managing reservoir sedimentation by venting turbidity currents: A review. *Int. J. Sediment Res.* 31 (3), 195–204. doi:10.1016/j.ijsrc.2016.06.001.
- Choux, C., Baas, J.H., McCaffrey, W.D., Houghton, P.D.W., 2005. Comparison of spatio-temporal evolution of experimental particulate gravity flows at two different initial concentrations, based on velocity, grain size and density data. *Sediment Geol.* 179, 49–69. doi:10.1016/j.sedgeo.2005.04.010.
- Crowe, C.T., Ttout, T.R., Chung, J.N., 1996. Numerical models for two-phase turbulent flows. *Ann. Rev. Fluid Mech.* 28, 11–43.
- Cossu, R., Wells, M.G., 2012. A comparison of the shear stress distribution in the bottom boundary layer of experimental density and turbidity currents. *European Journal of Mechanics - B/Fluids* 32, 70–79. doi:10.1016/j.euromechflu.2011.09.006.
- Davidson, J.F., Harrison, D., Carvalho, J.R.F.G.D., 1977. On the liquid like behavior of fluidized beds. *Annu. Rev. Fluid Mech.* 9 (1), 55–86. doi:10.1146/annurev.fl.09.010177.000415.
- De Cesare, G., Schleiss, A.J., Hermann, F., 2001. Impact of turbidity currents on reservoir sedimentation. *J. Hydraul. Eng.* 127 (1), 6–16. doi:10.1061/(ASCE)0733-9429(2001)127:1(6).
- de Leeuw, J., Eggenhuisen, J.T., Cartigny, M.J.B., 2018. Linking submarine channel-levee facies and architecture to flow structure of turbidity currents: insights from flume tank experiments. *Sedimentology* 65, 931–951. doi:10.1111/sed.12411.
- Dong, X., Tan, C., Yuan, Y., Dong, F., 2015. Oil-water two-phase flow velocity measurement with continuous wave ultrasound Doppler. *Chem. Eng. Sci.* 135, 155–165. doi:10.1016/j.ces.2015.05.011.
- Dorrell, R.M., Darby, S.E., Peakall, J., Sumner, E.J., Parsons, D.R., Wynn, R.B., 2014. The critical role of stratification in submarine channels: Implications for channelization and long runout of flows. *J. Geophys. Res.-Oceans* 119, 2620–2641. doi:10.1002/2014JC009807.
- Dorrell, R.M., Peakall, J., Darby, S.E., Parsons, D.R., Johnson, J., Sumner, E.J., Wynn, R.B., Ozsoy, E., Tezcan, D., 2019. Self-sharpening induces jet-like structure in seafloor gravity currents. *Nature Communications* 10, 1381. doi:10.1038/s41467-019-09254-2.
- Dombroski, D.E., Crimaldi, J.P., 2007. The accuracy of acoustic Doppler velocimetry measurements in turbulent boundary layer flows over a smooth bed. *Methods* 23–33. doi:10.4319/lom.2007.5.23.
- Downing, A., Thorne, P.D., Vincent, C.E., 1995. Backscattering from a suspension in the near field of a piston transducer. *J. Acous. Soc. Am.* 97 (3), 1614–1620. doi:10.1121/1.412100.
- Eggenhuisen, J.T., Tilston, M.C., Leeuw, J., Pohl, F., Cartigny, M.J.B., 2019. Turbulent diffusion modelling of sediment in turbidity currents: An experimental validation of the Rouse approach. *The Deposit Record* 1–14. doi:10.1002/dep2.86.
- Felix, M., Sturton, S., Peakall, J., 2005. Combined measurements of velocity and concentration in experimental turbidity currents. *Sedimentary Geology* 179 (1–2), 31–47. doi:10.1016/j.sedgeo.2005.04.008.
- Finelli, F., Hart, D.D., Fonseca, D.M., 1999. Evaluating the spatial resolution of an acoustic Doppler velocimeter and the consequences for measuring near-bed flows. *Limnol. Oceanogr.* Note 44 (7), 1793–1801. doi:10.4319/lo.1999.44.7.1793.
- Fisher, F.H., Simmons, V.P., 1977. Sound absorption in sea water. *J. Acous. Soc. Am.* 62 (3), 558–564. doi:10.1121/1.381574.
- Gladstone, C., Ritchie, L.J., Sparks, R.S.J., Woods, A.W., 2004. An experimental investigation of density-stratified inertial gravity currents. *Sedimentology* 51 (4), 767–789. doi:10.1111/j.1365-3091.2004.00650.x.
- Gore, R.A., Crowe, C.T., 1989. Effect of particle size on modulating turbulent intensity. *Int. J. Multiphase Flow* 15, 279–285.
- Gray, T.E., Alexander, J., Leeder, M.R., 2006. Longitudinal flow evolution and turbulence structure of dynamically similar, sustained, saline density and turbidity currents. *J. Geophys. Res.* 111, C08015. doi:10.1029/2005JC003089.
- Hitomi, J., Murai, Y., Park, H.J., Tasaka, Y., 2017. Ultrasound flow-monitoring and flow-metering of air-oil-water three-layer pipe flows. *IEEE Access* 5 (1), 15021–15029. doi:10.1109/ACCESS.2017.2724300.
- Hitomi, H., Nomura, S., De Cesare, G., Takeda, Y., Park, H.J., Tasaka, Y., Murai, Y., 2018. Flow monitoring of particle-laden flows combining ultrasonic Doppler and echo intensity profiling Techniques. 11th International Symposium on Ultrasonic Doppler Methods for Fluid Mechanics and Fluid Engineering.
- Hurthler, D., Thorne, P.D., Bricault, M., Lemmin, U., Barnoud, J., 2011. A multi-frequency Acoustic Concentration and Velocity Profiler (ACVP) for boundary layer measurements of fine-scale flow and sediment transport processes. *Coast Eng.* 58 (7), 594–605. doi:10.1016/j.coastaleng.2011.01.006.
- Kneller, B.C., Bennett, S.J., McCaffrey, W.D., 1999. Velocity structure, turbulence and fluid stresses in experimental gravity currents. *J. Geophys. Res.-Oceans* 104 (C3), 5381–5391. doi:10.1029/1998JC900077.
- Kneller, B., Buckee, C., 2000. The structure and fluid mechanics of turbidity currents: a review of some recent studies and their geological implications. *Sedimentology* 47, 62–94. doi:10.1046/j.1365-3091.2000.047s1062.x.
- Kneller, B., Nasr-Azadani, M.M., Radhakrishnan, S., Meiburg, E., 2016. Long-range sediment transport in the world's oceans by stably stratified turbidity currents. *J. Geophys. Res.* 121, 8608–8620. doi:10.1002/2016JC011978.
- Komori, S., Ueda, H., Ogino, F., Mizushima, T., 1983. Turbulence structure in stably stratified open-channel flow. *J. Fluid Mech.* 130, 13–26. doi:10.1017/S0022112083000944.
- Lee, T.H., Hanes, D.M., 1995. Direct inversion method to measure the concentration profile of suspended particles using backscattered sound. *J. Geophys. Res.* 100 (C2), 2649–2657. doi:10.1029/94JC03068.
- Lhermitte, R., Lemmin, U., 1994. Open-Channel Flow and Turbulence Measurement by High-Resolution Doppler Sonar. *J. Atmos. Oceanic Technol.* 11, 1295–1308. doi:10.1175/1520-0426(1994)011<1295:OCFATM2.0.CO>2.
- Luchi, R., Balachandar, S., Seminara, G., Parker, G., 2018. Turbidity currents with equilibrium basal driving layers: a mechanism for long runout. *Geophys. Res. Lett.* 45, 1518–1526. doi:10.1002/2017GL075608.
- McCaffrey, W.D., Choux, C.M., Baas, J.H., Houghton, P.D.W., 2003. Spatio-temporal evolution of velocity structure, concentration and grain-size stratification within experimental particulate gravity currents. *Marine and Petroleum Geology* 20 (6–8), 851–860.
- Meiburg, E., Kneller, B., 2010. Turbidity Currents and Their Deposits. *Ann. Rev. Fluid Mech.* 42, 135–156. doi:10.1146/annurev-fluid-121108-145618.
- Murai, Y., Matsumoto, Y., 2000. Numerical study of the three-dimensional structure of a bubble plume. *J. Fluid. Eng.* 122 (4), 754–760. doi:10.1115/1.1313245.
- Murai, Y., Oishi, Y., Takeda, Y., Yamamoto, F., 2006. Turbulent shear stress profiles in a bubbly channel flow assessed by particle tracking velocimetry. *Exp. Fluids* 41 (2), 343. doi:10.1007/s00348-006-0142-9.
- Murai, Y., Ohta, S., Shigetomi, A., Tasaka, Y., Takeda, Y., 2009. Development of an ultrasonic void fraction profiler. *Meas. Sci. Tech.* 20 (11), 114003. doi:10.1088/0957-0233/20/11/114003.
- Murai, Y., Tasaka, Y., Nambu, Y., Takeda, Y., 2010. Ultrasonic detection of moving interfaces in gas-liquid two-phase flow. *Flow Meas. Instrum.* 21 (3), 356–366. doi:10.1016/j.flowmeasinst.2010.03.007.
- Mulder, T.M., Alexander, J., 2001. The physical character of subaqueous sedimentary density flows and their deposits. *Sedimentology* 48 (2), 269–299. doi:10.1046/j.1365-3091.2001.00360.x.
- Murakawa, H., Kikura, H., Aritomi, M., 2008. Application of ultrasonic multi-wave method for two-phase bubbly and slug flows. *Flow Meas. Instrum.* 19 (3–4), 205–213. doi:10.1016/j.flowmeasinst.2007.06.010.
- Nagata, K., Komori, S., 2001. The difference in turbulent diffusion between active and passive scalars in stable thermal stratification. *J. Fluid Mech.* 430, 361–380. doi:10.1017/S002211200003037.
- Nomura, S., Hitomi, J., De Cesare, G., Takeda, Y., Yamamoto, Y., Sakaguchi, H., 2018. Sediment mass movement of a particle-laden turbidity current based on ultrasound velocity profiling and the distribution of sediment concentration 477, 427–437. doi:10.1144/SP477.19.
- Nomura, S., Hitomi, J., De Cesare, G., Takeda, Y., Yamamoto, Y., Sakaguchi, H., 2019. Sediment mass movement of a particle-laden turbidity current based on ultrasound velocity profiling and the distribution of sediment concentration. *Geological Society Special Publication*, p. 477. doi:10.1144/SP477.19.
- Nomura, S., De Cesare, G., Furuichi, M., Yasushi, Y., Sakaguchi, H., 2020. Quasi-stationary flow structure in turbidity currents. *Int. J. Sediment Res.* 35 (6).
- Oehy, C.D., De Cesare, G., Schleiss, A.J., 2010. Effect of inclined jet screen on turbidity current. *J. Hydraul. Res.* 48 (1), 81–90. doi:10.1080/00221680903566042.
- Oehy, C.D., Schleiss, A.J., 2007. Control of turbidity currents in reservoirs by solid and permeable obstacles. *J. Hydraul. Eng.* 133 (6), 637–648. doi:10.1061/(ASCE)0733-9429(2007)133:6(637).
- Pantini, H.M., 1979. Interaction between velocity and effective density in turbidity flow: phase-plane analysis, with criteria for autospension. *Marine Geology* 31 (1–2), 59–99. doi:10.1016/0025-3227(79)90057-4.

- Pantin, H.M., Franklin, M.C., 2011. Improved experimental evidence for autosuspension. *Sedimentary Geology* 237, 46–54. doi:10.1016/j.sedgeo.2011.02.002.
- Park, H.J., Tasaka, Y., Murai, Y., 2019. Bubbly drag reduction investigated by time-resolved ultrasonic pulse echography for liquid films creeping inside a turbulent boundary layer. *Exp. Therm. Fluid Sci.* 103, 66–77. doi:10.1016/j.exthermfluidsci.2018.12.025.
- Parker, G., Fukushima, Y., Pantin, H.M., 1986. Self-accelerating turbidity currents. *J. Fluid Mech* 171, 145–181. doi:10.1017/S0022112086001404.
- Peakall, J., McCaffrey, W.D., Kneller, B.C., 2000. A process model for the evolution, morphology and architecture of sinuous submarine channels. *J. Sediment Res.* 70, 434–448. doi:10.1306/2DC4091C-0E47-11D7-8643000102C1865D.
- Pedocchi, F., García, M.H., 2012. Acoustic measurement of suspended sediment concentration profiles in an oscillatory boundary layer. *Cont. Shelf Res.* 46, 87–95. doi:10.1016/j.csr.2011.05.013.
- Piper, D.J.W., Cochonot, P., Morrison, M.L., 1999. The sequence of events around the epicentre of the 1929 Grand Banks earthquake: Initiation of debris flows and turbidity current inferred from sidescan sonar. *Sedimentology* 46 (1), 79–97.
- Piccirillo, P., van Atta, C.W., 1997. The evolution of a uniformly sheared thermally stratified turbulent flow. *J. Fluid Mech.* 334, 61–86. doi:10.1017/S002211209600434X.
- Rice, H.P., Fairweather, M., Hunter, T.N., Mahmoud, B., Biggs, S., Peakall, J., 2014. Measuring particle concentration in multiphase pipe flow using acoustic backscatter: generalization of the dual-frequency inversion method. *J. Acoust Soc Am* 136 (1), 156–169. doi:10.1121/1.4883376.
- Rice, H.P., Fairweather, M., Peakall, J., Hunter, T.N., Mahmoud, B., Biggs, S.R., 2015. Particle concentration measurement and flow regime identification in multiphase pipe flow using a generalised dual-frequency inversion method. *Procedia Eng.* 102, 986–995. doi:10.1016/j.proeng.2015.01.221.
- Samothrakis, P., Cotel, A.J., 2006. Finite volume gravity currents impinging on a stratified interface. *Exp. Fluids* 41, 911–1003. doi:10.1007/s00348-006-0222-x.
- Schleiss, A.J., Franca, M.J., Jiménez, C.J., De Cesare, G., 2016. Reservoir sedimentation. *J. Hydraul. Res.* 54 (6), 314–595. doi:10.1080/00221686.2016.1225320.
- Sequeiros, O.E., Spinewine, B., Beaubouef, R.T., Sun, T., García, M.H., Parker, G., 2010. Characteristics of Velocity and Excess Density Profiles of Saline Underflows and Turbidity Currents Flowing over a Mobile Bed. *Journal of Hydraulic Engineering* 136, 412–433. doi:10.1061/(ASCE)HY.1943-7900.0000200.
- Sequeiros, O.E., Mosquera, R., Pedocchi, F., 2018. Internal Structure of a Self-Accelerating Turbidity Current. *J. Geophys Res-Oceans* 123, 6260–6276. doi:10.1029/2018JC014061.
- Shi, X., Tan, C., Dong, F., Murai, Y., 2019. Oil-gas-water three-phase flow characterization and velocity measurement based on time-frequency decomposition. *Int. J. Multiphas. Flow* 111, 219–231. doi:10.1016/j.ijmultiphaseflow.2018.11.006.
- Simmons, S.M., Azpiroz-Zabala, M., Cartigny, M.J.B., Clare, M.A., Cooper, C., Parsons, D.R., Pope, E.L., Sumner, E.J., Talling, P.J., 2020. Novel acoustic method provides first detailed measurements of sediment concentration structure within submarine turbidity currents. *J. Geophys Res-Oceans* doi:10.1029/2019jc015904, e2019JC015904.
- Simpson, J.E., Britter, R.E., 1979. The dynamics of the head of a gravity current advancing over a horizontal surface. *J. Fluid Mech.* 94 (3), 477–495. doi:10.1017/S0022112079001142.
- Simpson, J.E., 1997. *Gravity Currents: In the Environment and the Laboratory*. Cambridge University Press, Cambridge UK.
- Stacey, M.W., Bowen, A.J., 1988. The vertical structure of density and turbidity currents: Theory and observations. *J. Geophys. Res.* 93 (C4), 3528–3542. doi:10.1029/JC093iC04p03528.
- Su, Q., Chao, T., Feng, D., 2017. Mechanism modeling for phase fraction measurement with ultrasound attenuation in oil-water two-phase flow. *Meas. Sci. Tech.* 28 (3), 035304. doi:10.1088/1361-6501/aa58dc.
- Symons, W.O., Sumner, E.J., Paull, C.K., Cartigny, M.J., Xu, J.P., Maier, K.L., Lorenson, T.D., Talling, P.J., 2017. A new model for turbidity current behavior based on integration of flow monitoring and precision coring in a submarine canyon. *Geology* 45 (4), 367–370. doi:10.1130/G38764.1.
- Takeda, Y., 1995. Velocity profile measurement by ultrasonic Doppler method. *Exp. Therm. Fluid Sci.* 10 (4), 444–453. doi:10.1016/0894-1777(94)00124-Q.
- Takeda, Y., 2012. *Ultrasonic Doppler velocity profiler for fluid flow (Fluid mechanics and its applications)*. Springer, New York.
- Talling, P.J., Wynn, R.B., Masson, D.G., Frenz, M., Cronin, B.T., Schiebel, R., et al., 2007. Onset of submarine debris flow deposition far from original giant landslide. *Nature* 450 (7169), 541–544. doi:10.1038/nature06313.
- Talling, P.J., Masson, D.G., Sumner, E.J., Malgesini, G., 2012. Subaqueous sediment density flows: Depositional processes and deposit types. *Sedimentology* 59 (7), 1937–2003.
- Theiler, Q., Franca, M.J., 2016. Contained density currents with high volume of release. *Sedimentology* 63 (6), 1820–1842. doi:10.1111/sed.12295.
- Thomas, L.P., Dalziel, S.B., Marino, B.M., 2003. The structure of the head of an inertial gravity current determined by particle-tracking velocimetry. *Experiments in Fluids* 34, 708716. doi:10.1007/s00348-003-0611-3.
- Thorne, P.D., Hanes, D.M., 2002. A review of acoustic measurement of small-scale sediment processes. *Cont. Shelf Res.* 22 (4), 603–632. doi:10.1016/S0278-4343(01)00101-7.
- Xu, J., Swarzenski, P., Noble, M., Li, A.C., 2010. Event-driven sediment flux in Hueneme and Mugu submarine canyons, southern California. *Marine Geology* 269, 74–88. doi:10.1016/j.margeo.2009.12.007.
- Xu, J., 2010. Normalized velocity profiles of field-measured turbidity currents. *Geology* 38 (6), 563–566. doi:10.1130/G30582.
- Xu, J., Sequeiros, O., Noble, M., 2014. Sediment concentrations, flow conditions, and downstream evolution of two turbidity currents, Monterey Canyon, USA. *Deep Sea Research Part I: Oceanographic Research Papers* 89, 11–34. doi:10.1016/j.dsr.2014.04.001.
- Zordan, J., Schleiss, A.J., Franca, M.J., 2018. Structure of a dense release produced by varying initial conditions. *Environ. Fluid Mech.* 18 (5), 1101–1119. doi:10.1007/s10652-018-9586-8.